Atomic Magnetometry for the Detection of Cardio-magnetic Fields

A thesis submitted in partial fulfillment of the requirement
for the degree of Bachelor of Science with Honors in
Physics from William & Mary in Virginia,

by

Alexander T. Fay

Accepted for Honors

_____

Advisor: Prof. Eugeniy E. Mikhailov

_____

Prof. Irina Novikova

_____

Prof. Nahum Zobin

_____

Prof. Keith Griffioen

Williamsburg, Virginia
April 27th, 2019

Contents

Acknowledgments

I would first like to thank my advisor Eugeniy Mikhailov for never mincing words and Irina Novikova for passing this wonderful project down to me. I would like to thank Ravn Jenkins for her work on this project before me, were it not for her work, the project would not be where it is today. I would like to thank the Quantum optics Lab group for making me feel like I belong both as a scientist and as a friend. I would like to thank my family for their endless support of me in all of my pursuits and lastly I would like to thank Katy Savage for always supporting me and spending long nights helping me practice my talks. This work would not have been possible without the help of any one of these people.

List of Figures

List of Tables

Abstract

We demonstrate a method of measuring small constant gradients on top of a large constant background magnetic field using Electromagnetically Induced Transparency (EIT). The Earth provides a constant magnetic field of 25-50μT, and as such, measuring much smaller magnetic fields as well as smaller gradients presents a challenge often requiring special shielding. We show that by making use of common mode noise subtraction from a dual rail setup, our measurement is insensitive to these large fields, and in theory our method does not require shielding. Our dual rail setup allows us to measure small magnetic field gradients by utilizing EIT resonances in ^{87}Rb. In order to detect a cardio-magnetic field gradient, a magnetometer must be sensitive to gradients on the order of 10-100pT. Our setup has been found to be sensitive to magnetic field gradients as low as 400pT and we discuss potential future work that could be done to remove the necessity of shielding and produce greater sensitivity.

Chapter 1

Introduction

20th century advancements in magnetometer technology such as the Superconducting Quantum Interference Device (SQUID), which can measure very weak magnetic fields ($\approx$1fT), opened the door for doctors and medical scientists to examine the heart's magnetic field [1]. Called cardio-magnetic fields, they are created by the electric impulses generated by pacemaker cells inside a human heart during a heartbeat, that cause the muscle to expand and contract. The study of these fields has led to the birth of Magnetocardiology as a medical field, as mapping cardio-magnetic fields holds numerous possible benefits over the electronic cardiogram (ECG) method [2]. The ECG method, although effective, uses an array of sensors in direct contact with the patient to measure the electric potential across a number of points in the heart. This method has a few key drawbacks, namely that, because it measures only the electric potential magnitude between a few points, information about the current distribution on the heart throughout the beat is left out. It also requires direct contact with a patient's skin, which while usually a harmless process, can sometimes cause complications to occur.

The magneto-cardiograph (MCG) however, addresses many of the drawbacks of the ECG. Because it is a field, the magnetic field can be measured outside of

the patient's body, with the greatest magnitude of the field being just outside their chest. This means an MCG can be obtained entirely non-invasively, requiring no direct contact with the patient.

While the SQUID does present the ability to detect magnetic fields as low as $3fT$, it is costly as it requires a consistent supply of coolant to maintain superconduction, on top of the cost of superconducting materials such as Niobium or YBCO [2]. Furthermore, the SQUID only measures the magnitude of the magnetic field, losing all information about the directional components [3]. These limitations have led many to seek alternative methods through which weak biomagnetic fields can be measured.

Optical methods of magnetometry have been identified as one such alternative that has produced promising results, originally finding use in studies of geomagnetism, and measures of the Earth's magnetic field from space. They were also shown to produce promising results of small magnetic field measurements as far back as in the 1950s [4]. Methods taking advantage of the unique level structures of alkali-metals such as ^{87}Rb have been particularly effective, detecting fields as low as femtotesla [5, 6]. Methods of optical magnetometry have been successfully undertaken in an unshielded environment, and have also been miniaturized to a millimeter scale, developments that are beneficial towards creating a sensitive magnetometer for practical uses [7, 8]. Since the heartbeats magnetic field is within the range of $\approx$10-50pT, this defines our target sensitivity, therefore methods such as the one which is proposed here are a viable alternative to the SQUID for magneto-cardiograph (MCG) in medical science [2].

The goal of this project is to use atomic magnetometry to measure a pulsing cardio-magnetic field over a larger constant magnetic field on the order of the Earth's own magnetic field ($\approx 6\mu$T). The magnetometer used here operates utilizing the Zeeman effect, where the splitting of an atom's energy levels is proportional to the applied magnetic field. Because Electromagnetically Induced Transparency resonance location is dependent on the splitting of the energy levels due to magnetic fields, we can use the location difference of the peaks to determine the magnetic field applied.

By splitting the beam, and then propagating the pair through the field in two locations near each other, we can then take the difference of the signal, which will be proportional to the magnetic field gradient because the EIT resonances will be spilt differently due to the gradient in the field. To measure the EIT resonances we look for a peak in light transmission, which comes because the "transparency" of the Rubidium atoms creates a narrow "window" in the absorption line of the applied light fields. This is caused by special preparation of the Rb atoms and our light fields which will be discussed later on. Because the transmission peak is narrow ($<$ 10kHz) compared to the absorption line (500 MHz) the transmission peak allows us to measure the EIT resonances, and thus the splitting due to the magnetic field to a much higher degree of accuracy compared to measuring on the absorption line.

We are interested in testing the viability of this setup in a more realistic environment. In preparation for this, calibrations have been conducted to determine sensitivity and various contributing parameters have been optimized to increase our overall sensitivity. Following this the sensitivity of the magnetometer was probed using a quasi-static signal, and then the magnetometers response to arbitrarily shaped AC waveforms was also probed.

Chapter 2

Theory

Atomic magnetometer technology has improved in the last forty years by leaps and bounds, and has been a part of noteworthy experiments, such as being flown on a spacecraft to determine the geomagnetic field. With the integration of new research, in recent years, optical methods of atomic magnetometry are no longer peripheral techniques, they now have the sensitivity and accuracy to make them a novel approach towards incredibly small field detection. Within this section, the theory behind the operation of our atomic magnetometer will be discussed, with a focus on the methods that allow it to operate as sensitively as it can.

2.1   The Zeeman Effect

For any atomic magnetometer, the method of measurement for the magnetic field is centered around the Zeeman effect. The Zeeman effect describes how in the presence of a magnetic field, the initially degenerate energy levels of an atom will "split" into multiple levels based on their atomic numbers and the applied magnetic field as shown in Figure 2.1. This energy level splitting is linearly proportional to the magnetic field applied according to

$$\Delta E = \Delta m g \mu_B B, \tag{2.1}$$

where ΔE is the energy level splitting, g is the gyromagnetic ratio ($g = 2.0023193$), Δm is the spin difference between the atomic states, and $\mu_B = 1.399 * 10^{10} Hz/T$ is the Bohr magnetron, and B is the applied magnetic field [13].

In a perfect world, this would be enough to measure any magnitude of magnetic field by sweeping over the atom with an electromagnetic (EM) field and tracking the absorption spectra. However, when working with absorptions in the real world, one must contend with Doppler Broadening. Doppler Broadening refers to the broadening of absorption spectra in frequency space, as shown in Figure 2.2. Doppler Broadening makes it such that our absorption resonance which should have a line-width in the range of a few MHz, actually has a line-width that is hundreds of MHz wide [14]. Our theoretical sensitivity limit for detecting magnetic fields is based on how well we can resolve the splitting of the atomic energy levels. Applying Equation 2.1 and recalling that the hearts magnetic field is in the range of 10-100pT, we calculate that the energy level splitting in frequency space will be at most 1 Hz, and as low as .1 Hz. Since even a Doppler Broadening free absorption spectrum has line-widths on the order of MHz, it is clear that we will not be able to measure the hearts magnetic field using the absorption spectrum. To work around this issue we instead measure the Zeeman splitting via Electromagnetically Induced Transparency.

2.2   Electromagnetically Induced Transparency

Electromagnetically Induced Transparency (EIT) is an optical phenomenon whereby an atomic gas can be made to neither emit nor absorb electromagnetic fields, becoming effectively "transparent". Inducing EIT requires that the atom being used can be approximated as a three level system of an excited state and a ground state with hyperfine splitting [10]. ^{87}Rb is one such atom, and when it is addressed by
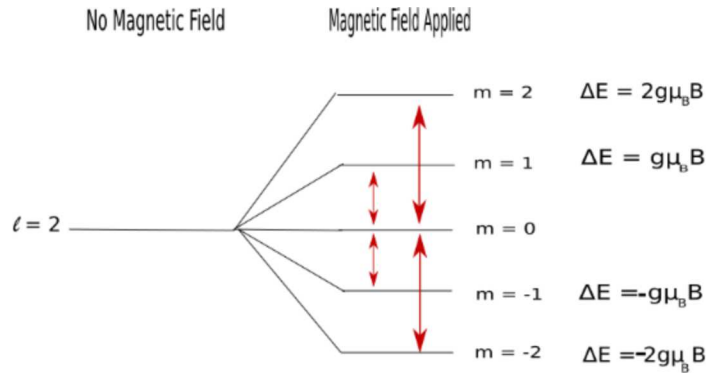
Figure 2.1: The Zeeman splitting for initially degenerate energy levels. It can be seen that for the $l = 2$ state, where we had one state initially we now have five states all occupying different energy states, with their splitting being proportional to the applied field.
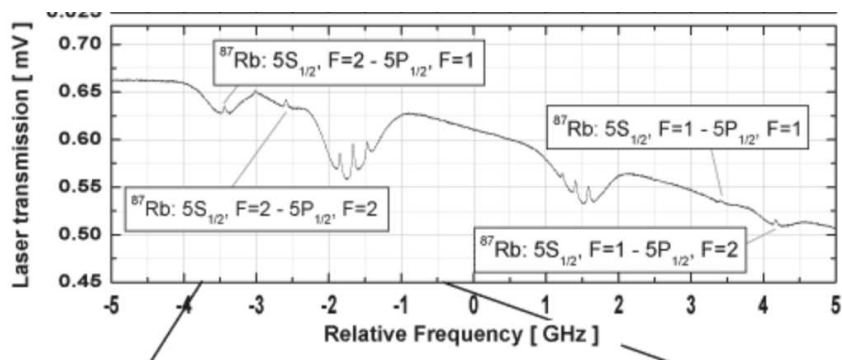

Figure 2.2: Absorption and transmission spectrum of Rb, modified from [14]. As can be seen from the line-shapes in this spectrum, the natural line-width of Rb is in the hundreds of MHz.
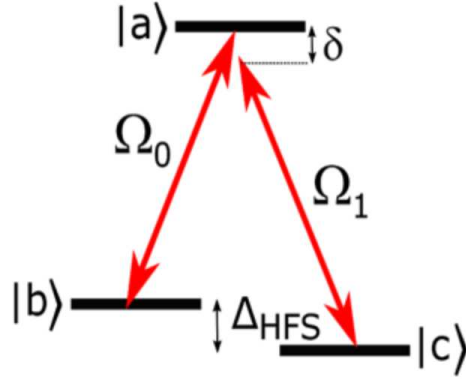
Figure 2.3: A three level lambda system, where the frequency difference between the two EM fields, also called the two photon detuning, is equivalent to the hyperfine splitting in the ground state. This couples the fields between each ground state and the excited state. Figure modified from Reference [9]

two electromagnetic (EM) fields, we can couple the fields to the two ground states by achieving two photon resonance which is defined as

$$\delta = (\omega_1 - \omega_0) - \omega_{bc} = 0, \tag{2.2}$$

where ω_2 and ω_1 are the frequencies of the EM waves and ω_{bc} is the frequency difference between ground states b and c of the atom as shown in 2.3, and δ is the two photon detuning [9]. When two photon resonance is achieved, our level structure appears as shown in 2.3 and our three level system will become artificially transparent. While a full examination of this phenomena requires the use of density matrix formalism, EIT is notable in that one can glean the basics of its physical operation from Time-Dependent Perturbation Theory using methods available in a college undergraduate's textbook such as [11]. A detailed derivation via this method is available in my predecessor Kevin Cox's previous work on this project [3], so it will be covered in brief here.

To determine the conditions for EIT, one solves the Time Dependent Schrdinger Equation for the three level system in the approximation of a small perturbation

H' to the initial atomic Hamiltonian. Solving the resulting matrix equation using Time Dependent Perturbation Theory for the case of two EM fields interacting only with their coupled states, our matrix equations simplifies down to a system of three equations:

$$i\dot{c_a} = \Omega_1 e^{i(\omega_1 - \omega_{ab})t} c_b + \Omega_0 e^{i(\omega_2 - \omega_{ac})t} c_c, \tag{2.3}$$

$$i\dot{c_b} = \Omega_1 e^{i(\omega_2 - \omega_{ab})t} c_a, \tag{2.4}$$

$$i\dot{c_c} = \Omega_1 e^{i(\omega_1 - \omega_{ac})t} c_a. \tag{2.5}$$

Where c_a, c_b, and c_c represent the coefficient of probability for states a, b, and c. From these three equations, we now want to solve for the condition where $\frac{\partial}{\partial t} c_a$ is zero, corresponding to no exchange of atoms in or out of the excited state. This further simplifies our system of three equations to a single equation,

$$\Omega_1 c_b = -\Omega_0 c_2 e^{i[(\omega_2 - \omega_{ac}) - (\omega_1 - \omega_{ab})]t}. \tag{2.6}$$

From this equation we recover our earlier result in different notation: that the difference in laser frequencies must be equal to the difference in energy levels b and c, in our case the two ground state energy levels to induce two-photon resonance. It further implies by nature of its derivation that no atoms in the ground states will be excited into the excited state a, which achieves our goal of inducing EIT. Taking into consideration constraints on the population distribution and solving for the coefficients of each state, we find that our system is in a superposition of two quantum states, a bright state $|B>$ and a dark state $|D>$, given by:

$$|B> = \frac{1}{\sqrt{\Omega_0^2 + \Omega_1^2}} (\Omega_1 |b> + \Omega_0 |c>), \tag{2.7}$$

$$|D> = \frac{1}{\sqrt{\Omega_0^2 + \Omega_1^2}} (\Omega_1 |b> - \Omega_0 |c>). \tag{2.8}$$

Up until now we have solved everything in the approximation of Time Dependent Perturbation Theory [3, 11]. Density Matrix Formalism introduces the final and arguably most important part of EIT, which is spontaneous emission from the interaction with the vacuum EM field. Qualitatively, what this consideration adds to this system is the following: an atom, once excited by the EM field will decay into either the Bright of the Dark state, if it decays into the Dark state it will not be re-excited. However, if it decays into the Bright state it has the chance to be excited again, at which point it can once again decay into either the Bright or the Dark state. By this process over time, all atoms will eventually end up in the Dark state, and will not be re-excited. Because of the nature of this process EIT is sometimes also called Coherent Population Trapping (CPT).

What makes EIT such a useful experimental technique is that it has a line-width that is thinner than the line-width of an absorption line with or without doppler broadening, since the line-width for an EIT resonance is related to the lifetime of the atomic state. Theoretically for a pure system, the lifetime would be infinite and our resonances would be infinitely sharp, but due to vacuum field interactions the atomic state that produces EIT will begin to decay shortly after it leaves the beam. To keep our lifetimes long and our resonances sharp we use special techniques which will be discussed in later chapters to keep atoms interacting with the beams longer.

Since the conditions for EIT require that the laser fields be coupled between one of the ground states and the excited state in question, when we introduce a magnetic field to our atom, we split the excited state into multiple states, now with different frequencies. This excited state splitting essentially creates multiple lambda systems that now have the potential to induce EIT as seen in Figure 2.4a. If we were to sweep our frequency over an appropriate range, where we once saw a single EIT resonance,

we would now see multiple, corresponding to the split energy states as displayed in Figure 2.4b. Furthermore, just like directly measuring a magnetic field via the Zeeman effect, the distance between the centers of these EIT resonances would be linearly proportional to the magnetic field being applied. Thus EIT allows us to make indirect measurements of the Zeeman effect, and thus the magnetic field, and as can be seen in Figure 2.5 has the benefit of not encountering the same broadening that is seen in absorption spectra. This effectively takes our frequency space resolution from hundreds of MHz into the range of kHz, increasing our overall sensitivity by a factor of 10^3 - 10^6.

(a)   (b)
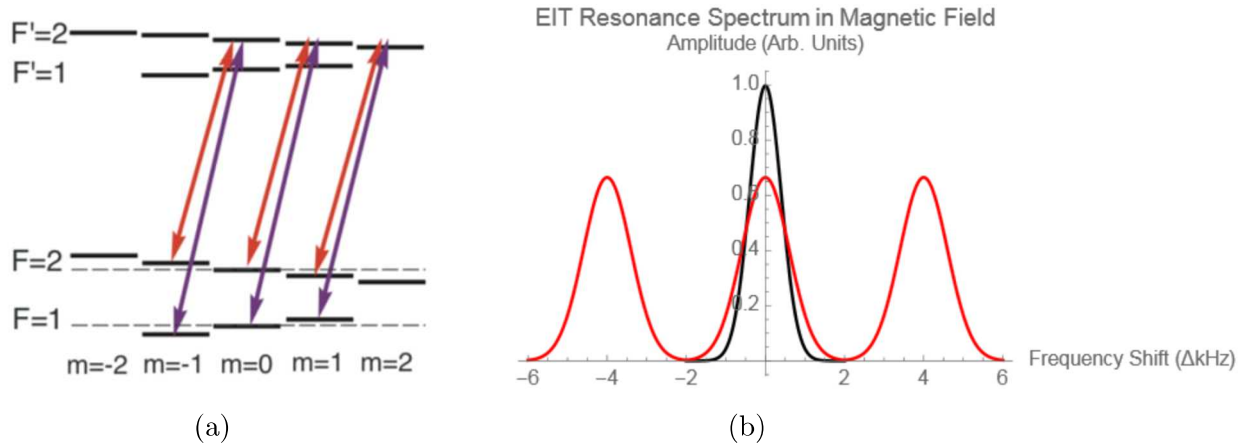
Figure 2.4: a) The multiple lambda systems that emerge under the application of a magnetic field due to the Zeeman effect, allowing for multiple EIT resonances to be seen. Modified from [12]. b) Simulation data displaying the result of the Zeeman effect applied to EIT resonances, with the black trace representing no applied magnetic field, and the red representing an applied magnetic field. Where there was once only a single resonance in the center, there are now three resonances spaced out by a frequency difference.

Figure 2.5: An example EIT resonance compared to a normal absorption resonance modified from [10]. This figure makes plainly clear the improvement in frequency resolution that can be obtained through the use of EIT

2.3 Differential Measurements and Magnetic Field Gradients

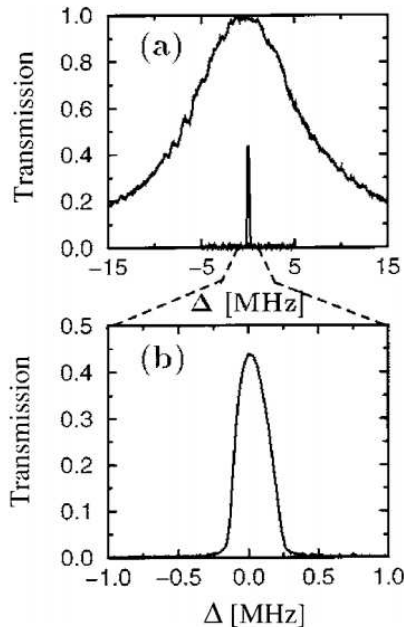Up until this point we have been purely considering magnetic fields that are held constant in space and time. However, to further bolster the sensitivity of our magnetometer we make use of an important characteristic of small magnetic fields such as those created by the human heart: its spatially variant nature. The magnetic field of the human heart is strongest immediately surrounding the heart, and from there its magnitude decreases as you measure farther and farther away.

By tuning our system to look exclusively for this behavior, we can isolate ourselves from a great deal of ambient magnetic fields and the noise they introduce. In practice, this is done by splitting our beam such that we have two beams that probe

11

the atoms in an area that is slightly separated spatially, and on the other end we have a detector that takes the difference of the two beams, which we call separate "rails". This means that any noise, or magnetic interference that is "seen" by both of the beams is subtracted off at the detection stage, and as a result we will see a differential signal that is proportional to the gradient in the magnetic field, as shown in Figure 2.6. Utilizing this proportionality allows us to greatly increase our sensitivity and remove large constant magnetic fields from consideration.
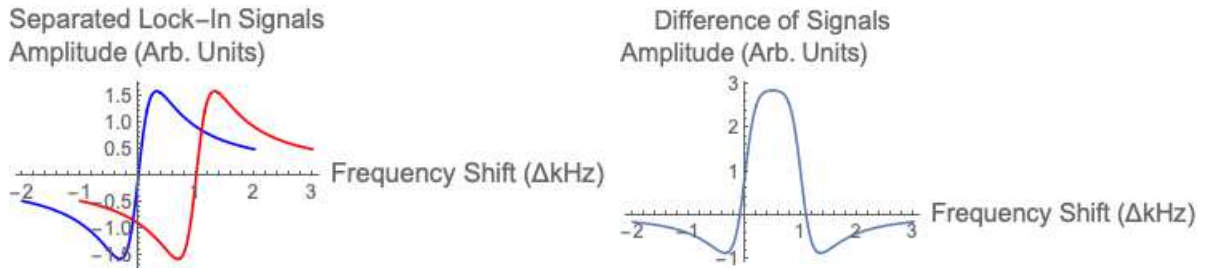

Figure 2.6: Two signals shifted slightly from one another, such as in the case of a gradient interaction when subtracted from one another produce the resulting signal. The size of this signal is proportional to the distance between them, and thus we can use the size of the signal as a measurement of the spacing and gradient.

Chapter 3

Experimental Technique

Having covered in detail the theory behind the operation of the magnetometer, we will now discuss the experimental techniques employed to execute this theory in reality. Within this section, we will begin by covering the apparatus itself and the operation of the various components. Then we will move on to a discussion of the methods used to tune and prepare the system for real experimental work. Included within will also be a discussion of a new detector circuit that has been integrated into the setup to streamline data collection. A number of important experimental parameters are contained within Table 3.1.

Table 3.1: A table containing some useful experimental parameters that contribute to the operation of our magnetometer.

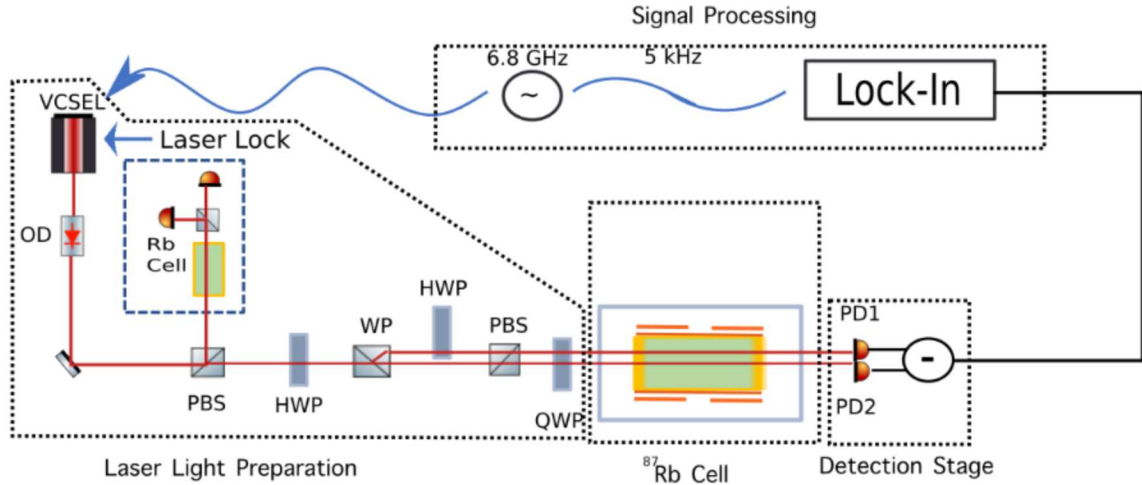|	
VCSEL Frequency	^{87}Rb D1 line 795nm
^{87}Rb Hyperfine Splitting	6.834 GHz
^{87}Rb Cell Dimensions	length 10mm, diameter 22mm
Zeeman Splitting due to Solenoid Field	34.09 $\frac{\Delta kHz}{mA}$
Gradient Coil Conversion Factor	97 $\frac{nT}{V \cdot d}$

Figure 3.1: Our setup schematic for the detection of differential signals. In general it has four separate stages: Laser Light Preparation, [87]Rb cell, Detection, and Signal Processing. OD is for Optical Diode, PBS is for Polarizing Beam Splitter, HWP is for Half Wave-Plate, WP is for Wollaston Prism, QWP is for Quarter Wave-Plate, and PD is for PhotoDiode.

3.1   Apparatus Design

Overall, our experimental apparatus, as depicted in Figure 3.1, can be separated into four components: the light source, the Rb cell, the detection stage, and finally the signal processing stage. The light source is where we prepare the beam for EIT, the Rb cell is where the beams are interacting with the [87]Rb, and the detection stage is where our EM fields are converted into electrical signals that can be interpreted using laboratory equipment

3.1.1   Laser Light Preparation

The laser light preparation portion of our setup, shown in Figure **??**, begins with a Vertical Cavity Surface Emitting Laser (VCSEL) tuned to the [87]Rb D1 line at $\approx$ 795nm. As depicted in Figure 2.3 however, we need two EM fields to achieve two photon resonance and induce EIT in the atom. Obtaining the exact frequency difference necessary while also sweeping frequencies over a range using two individual

lasers would be cumbersome, difficult, and inaccurate. Instead we create multiple EM fields by current modulating our VCSEL laser at the hyperfine splitting frequency of ^{87}Rb $\Delta_{HFS} \approx 6.834 GHz$ with an RF generator. This current modulation of the laser acts as a frequency "comb", creating sidebands along the original EM wave which oscillate at a frequency differing from the original by integer multiples of the modulation frequency. This means that our original EM wave can be paired with either the higher or lower sideband, and still induce EIT. By using this method we avoid using extra lasers, and can be assured that our EM fields are always in two photon resonance, so long as they are driven by the correct frequency.

Moving on from the VCSEL laser, our beam is passed through an Optical Diode (OD) which is used to ensure that there is no beam reflected back into the laser, which would introduce interference and distortion. The beam then goes through a Polarizing Beam Splitter (PBS). This PBS is used to split a small amount (10-20%) of the laser light into our Dichroic Atomic Vapor Laser Lock (DAVLL). The DAVLL's purpose is to act as a frequency reference for our VCSEL laser because although VCSEL lasers are incredibly useful for our apparatus and experiment, they have a critical downside. The frequency of light that they output tends to vary and drift as much as MHz over time simply from temperature changes and other interferences one might typically find in a physics laboratory. In order to combat this frequency drift the DAVLL serves as a reference frequency to lock the VCSEL. Its method of operation is discussed in detail in [15] and [16], but in essence it operates by using a differential detection scheme to create an electrical feedback signal around various transitions in Rb as shown in Figure 3.2. Thus by using the appropriate circuitry, this electrical feedback signal can be used to correct the lasers position any time that it drifts from the desired transition.
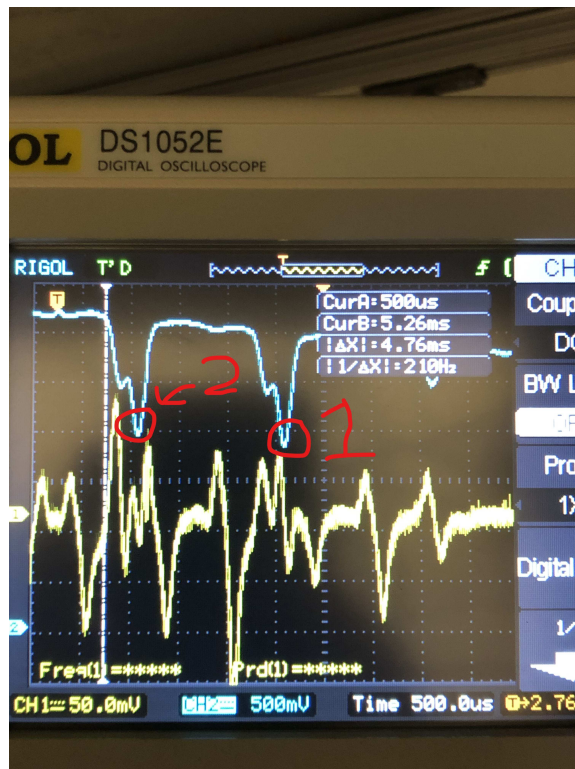
Figure 3.2: An annotated picture of our DAVLL output taken in the laboratory. The blue trace represents that absorption spectrum of Rb, giving us a reference to lock against, the yellow trace is the electrical feedback signal used to lock our laser. The 1 and 2 on the screen both represent that F = 2 to F = 1 transition in ^{87}Rb, with the carrier frequency of our EM wave locked to a different ground state. Both of these transitions were probed for their sensitivity which is discussed in a later section.

After the PBS and the DAVLL, our beam goes through a Half Wave-Plate (HWP) which is used for intensity optimization. From the HWP the beam is sent into a Wollaston Prism (WP) which is used to split our beam into two separate beams that are parallel to one another, and separated by about .4cm. This is to create our Dual Rail design and allow for differential detection of gradients. The two beams then pass through another HWP for the purpose of matching the relative intensities of the two, or in practice, accounting for any misbalancing at the detection stage. After the HWP, there is a PBS to ensure that both beams have the same polarization, and a Quarter Wave-Plate (QWP) which is used to circularly polarize our beams.

3.1.2 ^{87}Rb Cell

With our beam fully prepared to induce EIT, it now enters the μ metal magnetic shield. Although our setup should theoretically be able to operate without shielding, to ensure that any interfering fields are predictable, we use the magnetic shielding. Inside the magnetic shield we have a gradient coil, a solenoid, and the Rb cell itself which is attached to a heating element which is used to heat the Rb to 75° Celsius. The Rb cell is a pyrex cylinder with a length of 10mm and a diameter of 22mm. Inside the cell the Rb is in a liquid and saturated vapor form, alongside 5 Torr of Ne gas. The Ne gas serves as a buffer agent to increase the amount of time that an Rb atom is in the path of the beam, as this is directly related to the line-width of our resonances. The solenoid and gradient coils are used to create large constant magnetic fields, and spatially variant magnetic fields for the purpose of characterizing and calibrating the response of our magnetometer. The operation and function of these coils is covered in later sections within this chapter.

3.1.3 Detection Stage

In previous iterations of this experimental setup, the detection stage consisted only of a differential detector known as the Balanced Photodiode (BPD) V4 designed and constructed by Professor Eugeniy Mikhailov which is displayed in 3.3a. In theory this is all that our experimental apparatus requires to run. However, in practice, for operations such as calibrations and optimizations, where one may need the single input of one channel, or even the sum of the two, it required the tedious process of covering a rail and recording, then covering the other and recording again, before adding the two manually. To streamline this process, we developed a new detector circuit that has the added ability to record not only the difference of the two inputs, but also the sum, and the individual values for each rail as well. This detector, shown in Figure 3.3b has been named the Adding-Subtracting Photo-Electric Circuit with Transimpedance (ASPECT) V1.17, and it has been successfully implemented into the detection stage, and operates as well as the previous design.

The operation of the circuit is fairly simple, as it is mainly composed of operational amplifier circuits. A block diagram for the ASPECT is shown in Figure 3.4, in essence it consists of a pre-amplification stage, where the currents from the photodiodes, which is on the order of microamps, is converted into a voltage on the order of millivolts that can be used by later stages, and by the instruments we have available in the lab. Since the most important output for our experiment is the differential signal, the first operation that the ASPECT undertakes is a subtraction operation, so that we may avoid introducing any extra electrical interference or misbalancing. After this each rail goes through a buffer amplifier, and then off to its own individual channel output. The final operation conducted by the ASPECT is the summation of the two signals.
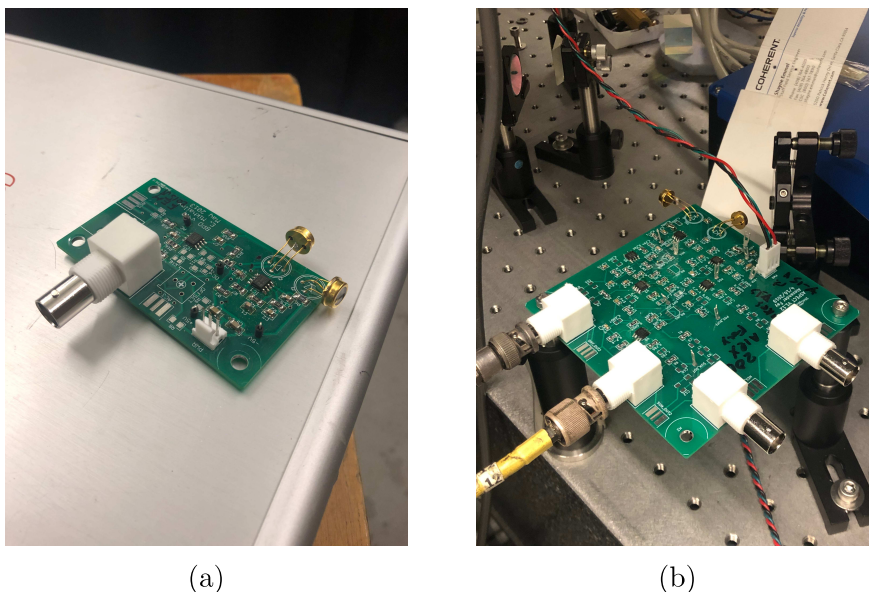
(a)   (b)

Figure 3.3: a) The detector circuit used in previous iterations of this experimental setup. As can be clearly seen it was designed for the singular purpose of taking the difference signal of the two EM fields and outputting them. b) The detector circuit currently in use within the magnetometer. Due to the increase in the number of operations being completed the complexity of the board has increased, however, as can be seen it provides a much larger range of possible output signals.
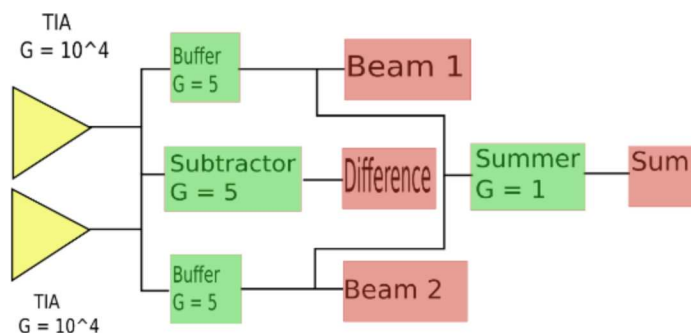

Figure 3.4: Block Diagram displaying the method of operation for the ASPECT V1.17. Each block in the diagram essentially represents an operational amplifier circuit that conducts the implied operation, amplifying the signal by a gain factor at each point.

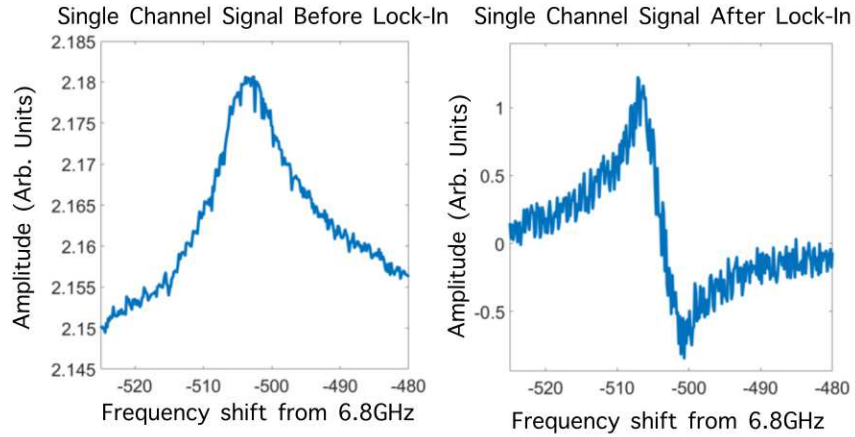Single Channel Signal Before Lock-In   Single Channel Signal After Lock-In

Figure 3.5: An EIT transmission resonance recorded on the scope before and after it was filtered through the lock in amplifier modified from [9]. In this figure it is easy to see that the Lock-In amplifier computes the derivative of the input.

3.1.4 Signal Processing

After the detection stage, our differential signal is fed into a Lock-In amplifier. The Lock-In amplifier serves both as a signal amplifier, and as a second round of noise filtering. The Lock-In amplifier operates by imposing a frequency "dither" on the driving frequency of our VCSEL laser. While imposing the "dither" it probes the magnitude of the response of the differential signal, essentially obtaining the derivative of the differential signal that if fed into it. This result is displayed in Figure 3.5.

3.2 Magnetic Field Generation

Since our magnetometer is currently contained within a magnetic shield, we need to use various coils to create the magnetic field when characterizing our magnetometers response. The first coil is the solenoid, used to make large constant magnetic fields along the direction of beam propagation. Second are the gradient coils which are used to create a magnetic field gradient that is perpendicular to the direction of beam propagation. They will be discussed in detail herein.
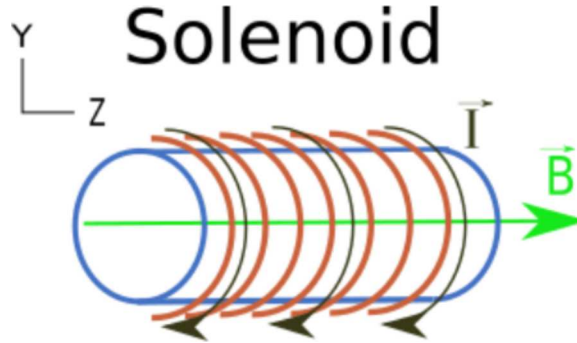
Figure 3.6: The method of operation of a solenoid. The coils are wrapped around a cylinder, and current is run clockwise through the wires to create constant magnetic field in the direction of beam propagation, in this case the Z direction.

3.2.1 Solenoid Operation

A solenoid is a simple electrical circuit, the operation of which is shown in Figure 3.6. The solenoid creates the magnetic field we need when we run current clockwise along the coils, and the strength of the resulting constant magnetic field will be given by

$$B = \mu_0 dI. \tag{3.1}$$

Where μ_0 is the Vacuum Permeability, d is the density of the coils $\left(\frac{n}{l}\right)$, and I is the current applied the to coils.

3.2.2 Solenoid Calibration

Both as a test of the magnetometer and of the solenoid itself, we calibrated the solenoid magnetic field by varying the current applied, and measuring the splitting of in location of the transmission resonances as displayed in Figure 3.7a while operating in single rail mode. We expect that when we then plot the splitting of transmission resonances against the applied current (magnetic field) we will see a linear relationship. This plot is shown in Figure 3.7b, and we recover this linear relationship in our calibration.

21
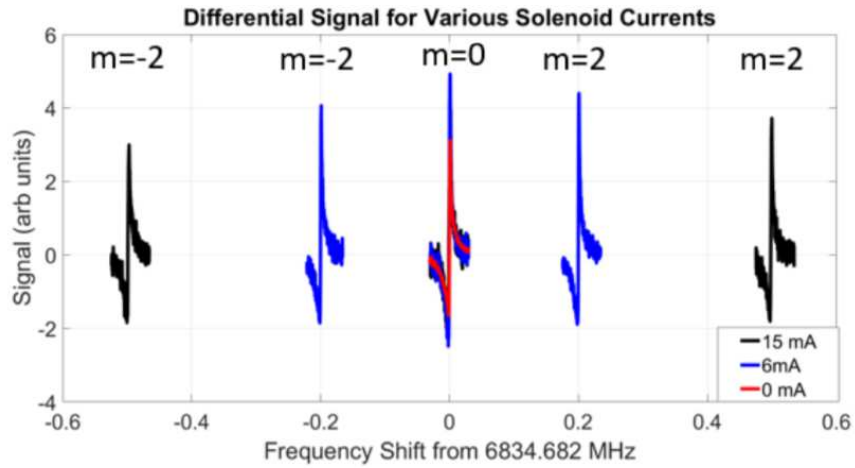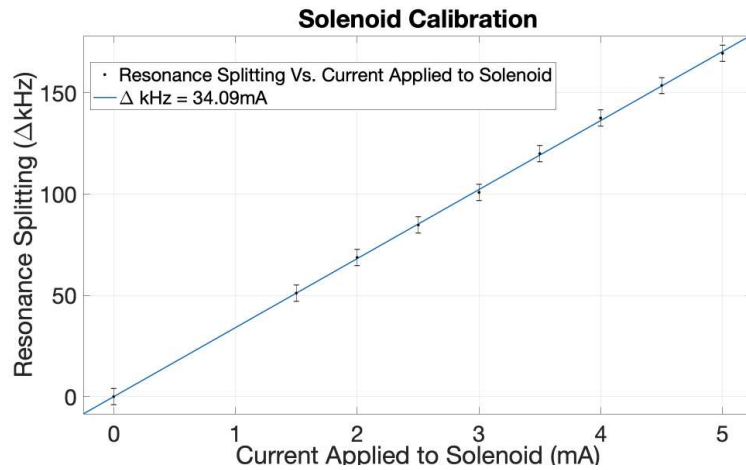
Figure 3.7: a) A collection of traces captured on oscilloscope at different levels of current applied in the solenoid. As can be seen, as we increase the current, and thus the constant magnetic field, we go from a single resonance to multiple, with a spacing between them that increases with increasing magnetic field. b) Results of our calibration of the solenoid. As can be seen, we recover the expected result of a linear relationship between applied current, and transmission resonance splitting, and when there is zero applied field, our splitting is also equal to zero.

3.2.3   Gradient Coil Operation

The operation of the gradient coils, as compared to the solenoid is slightly more complicated. In previous iterations of this setup, single and double wire gradients were used to create measurable magnetic field gradients. The magnetic fields created by these setups created a magnetic field according to

$$B = \frac{\mu_0 I}{2\pi r}. \tag{3.2}$$

However, the problem with these setups was that when the fields created by the wires were projected perpendicular to the propagation direction of the beam, the total field magnitude given by

$$B_{Total} = \sqrt{B_{Gradient}^2 + B_{solenoid}^2}, \tag{3.3}$$

had a quadratic fall-off with respect to distance from the wire. Since we are looking to categorize linear gradients, it was clear a new setup was needed. From Equation 3.3 we can seen that so long as we have perpendicular magnetic fields, obtaining a linear gradient will be difficult. To address this concern, we designed and engineered a set of coils which would be able to create a magnetic field in the direction of beam propagation, that had a linear spatial gradient perpendicular to the propagation direction.

The design we ended up settling on, displayed in 3.8a, is presented in [17], and consists of two pairs of rectangular "saddle" coils fitted around the cylinder as displayed in 3.8b. An interesting aspect of these coils is that their design is derivative of the gradient coils used in MRI machines, although modern MRI machines use advanced designs with considerably increased signal fidelity. For our purposes a first order design was sufficient to fulfill the role.
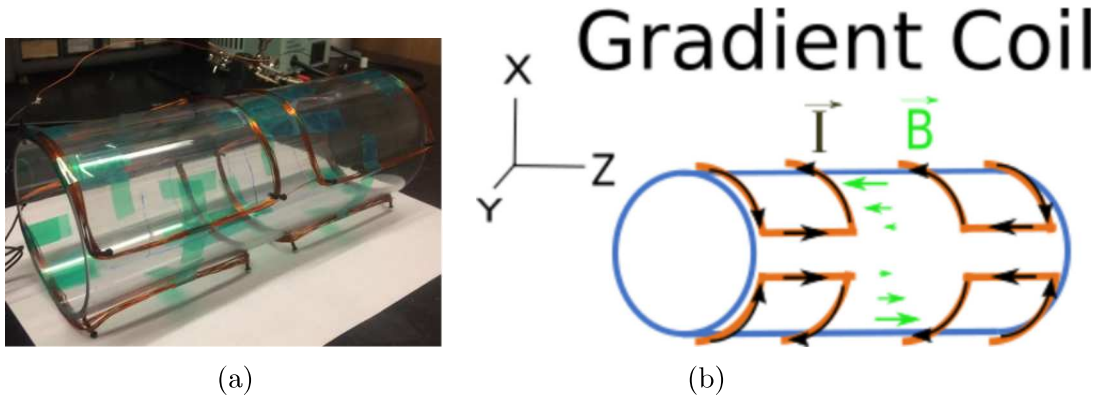
Figure 3.8: a) The gradient coils used to create magnetic field gradients within the magnetic shield. The design is based off of the MRI technology proposed in [17]. b) The gradient coils contained within the magnetic shield. They operate by having a current run clockwise in one pair, and counterclockwise in the other pair. This generates a magnetic field in the Z direction (propagation direction) which has a spatial gradient in the x direction.

3.2.4 Gradient Coil Calibration

To test that the gradients created by these coils are indeed linear, and to calibrate the magnetic field gradients produced by them, we measured the difference in frequency position of the same transmission resonance as seen by each individual channel. Again, if the coils work as expected we expect to see a linear relationship, the results are plotted in 3.9. We see the expected linear relationship, and furthermore we can take this linear relationship and convert it into a magnetic field gradient, telling us exactly what magnetic field gradients we are supplying based on the voltage we supply.

To convert our calibration result into a magnetic field we use the Zeeman effect for Rb, which translates to $7 \cdot 10^9 |\Delta m|$ Hz/T. Considering we are probing the Δm = +/- 2 transitions, this gives us a conversion factor of $1.4 \cdot 10^{10}$ Hz/T. Applying this conversion factor we find that our gradient coils provide magnetic field gradients according to $97(\frac{nT}{V \cdot d})$. With this calibration, we now know exactly what magnitudes
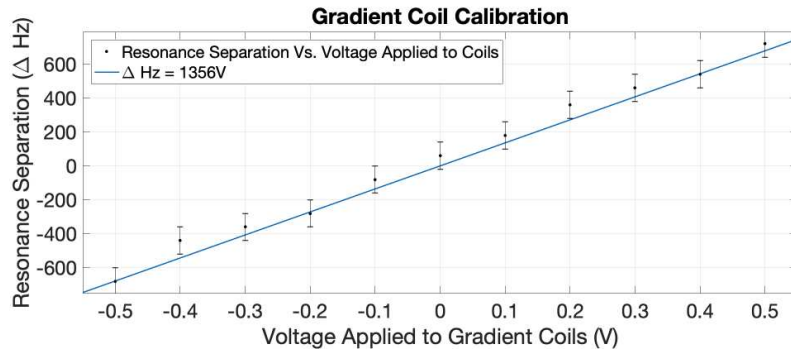
24

Figure 3.9: Results of the Gradient Coil Calibration. As we expected we find a linear relationship between the current applied to the gradient coils and the frequency separation of a single transmission resonance.

of magnetic field gradients we are creating when we apply a voltage to our gradient coils.

Chapter 4

Optimizations

Aside from all of the necessary calibration work with our magnetic field generation techniques, optimizations of various parameters is also necessary to reduce the interference of noise and bring our magnetometer to the necessary sensitivity level. The most important optimization parameters that we examined within our setup were the QWP angle, Lock-In amplifier settings, and the temperature of the Rb cell. The full results of our optimization is contained within Table 4.1

Table 4.1: Our optimized values for the magnetometer. The details of their acquisition are provided in depth in Appendix A.

Quarter Wave-Plate Angle	70°
Lock-In Amplitude	1V
Lock-In Frequency	5kHz
Lock-In Time Constant	3ms
Rb Cell Temperature	75°C

4.1   Quarter Wave-Plate Optimization

The QWP as mentioned earlier will affect the amplitude of different modes of light depending on its angle. Due to selection rules only certain polarizations of light will interact with our system in a way that contributes. Thus depending on
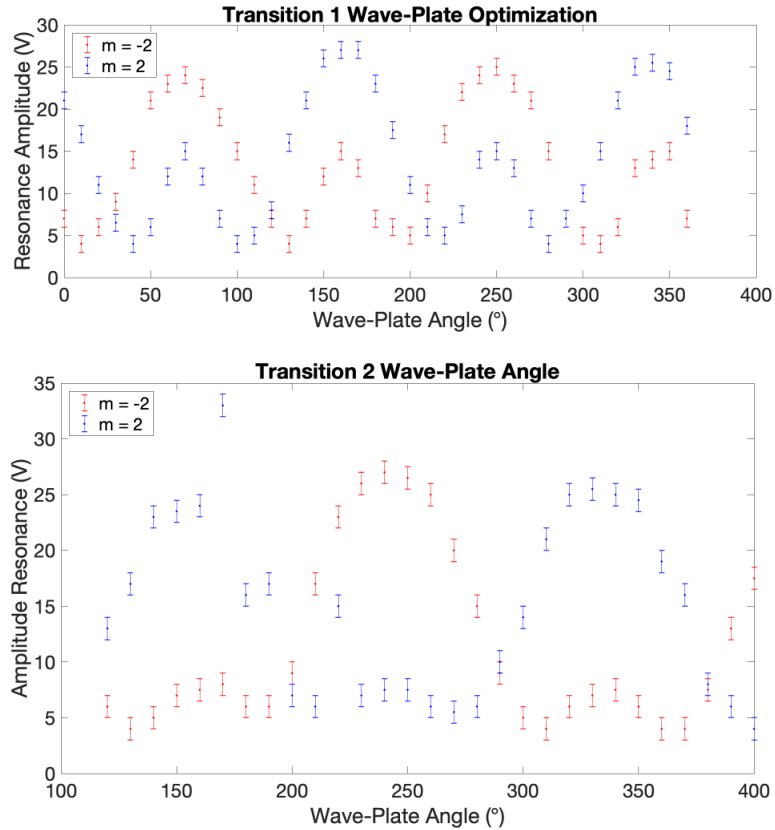
Figure 4.1: Results of optimizing the quarter wave-plate angle for our setup on transitions 1 and 2. Although a similar response was seen on both transitions, transition 1 provided for a stable laser lock as compared to the transition 2, and as such it was chosen to be used for this experiment.

the polarization of our wave plate, we can maximize or minimize the amplitude of our transmission resonances. This implies that there exists a theoretical ideal angle for the light modes that we are using. To determine this ideal value, the angle of the wave-plate was varied while in single rail mode, and the heights of the various transmission resonances were recorded across transition 1 and 2 as shown in Figure 3.2. The data for this optimization is located in Figure 4.1.

From this dataset, we determined that both transitions provided a similar response, however, transition 1 resulted in a more stable laser lock so it was chosen for the experiment. The transmission resonance corresponding to the $m = -2$ state on

transition 1 yielded the greatest sensitivity when the QWP was set at an angle of 70°. Transition 2 showed promising results for the m = 2 resonance around 150°, however, due to the large number of absorptions in that region of the atomic spectrum of natural abundance Rb vapor the laser lock was fairly unstable. and we were unable to maintain a lock long enough for it to be feasible.

4.2   Lock-In Amplifier Optimization

The Lock-In amplifier has a number of parameter that it uses when filtering incoming signals that we can optimize for. The frequency dither that the Lock-In amplifier supplies comes in the form of a sine wave, so many of our optimization parameters center around the qualities of this sine wave. Namely we want to optimize the amplitude, and frequency of the sine wave. Aside from this value, we also want to optimize the time constant of the Lock-In amplifier, which essentially sets the time period over which the Lock-In will integrate the data, acting as an RC filter.

Optimization of the amplitude and the frequency was done by varying the parameter with the others held constant, while recording the amplitude of the transmission resonance. We found the ideal frequency to be about 5kHz. The resonance amplitude with respect to the amplitude of the Lock-In is show in Figure 4.2. The ideal time constant was determined by analyzing our Lock-In output with all other parameters held constant, and picking out the time constant that reduced the most noise without disrupting the signal we were trying to detect, and this was determined to be 3ms.
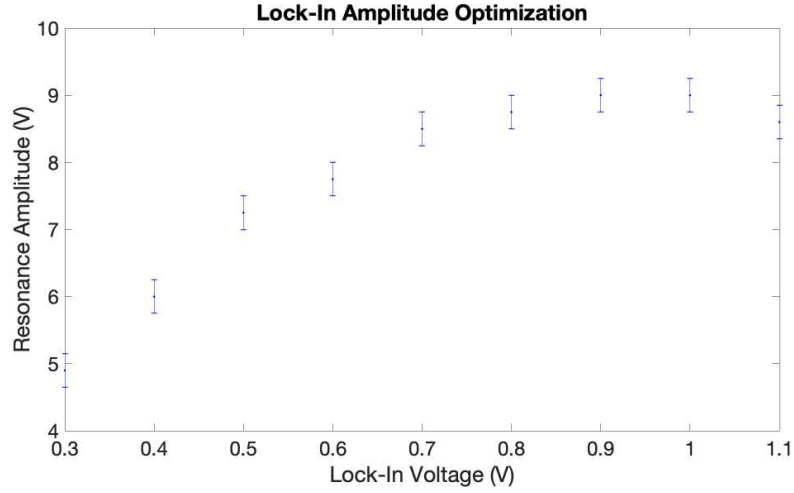
Figure 4.2: Results of the optimization of the Lock-In Amplifier amplitude. From this plot it is clear that around .9-1V is our ideal amplitude

4.3 Temperature Optimization

Finally, it has been noted in the last iteration of this experiment that an important area of further optimization may be in the temperature at which the Rb cell is kept [9]. This is because the amplitude of our transmission resonances is linked to the number of Rb atoms interacting with our beams. A simple way to increase the number of atoms interacting is by increasing the amount of Rb that we are vaporizing. However, there is a downside to this as well, at a certain point enough Rb atoms will be interacting that, because our EIT is not perfect, the combined absorption of all interacting atoms will deplete our laser field resulting in a decrease in our transmission resonance strength.

This means that there will be a "sweet spot" of sorts in between the two extremes. To identify the location of this sweet spot, we swept the temperature of the Rb cell through a range of 40°C to 90°C, while recording the amplitude of our signal in dual rail operation. The response of our magnetometer can be seen in Figure 4.3. From this testing it was identified that we have a maximum signal at $\approx 75°$C.
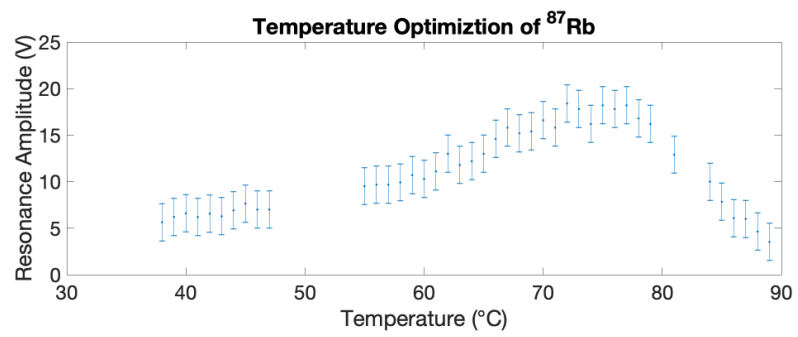
Figure 4.3: The signal dependence on temperature at which the Rb cell is kept. Missing data points are the result of the discovery that our thermometer was lagging behind the actual temperature of the cell.

Chapter 5

Magnetometer Response to Gradients

Having completed all of the preparatory work on the magnetometer, we moved on to work analyzing the magnetometers response to magnetic field gradients. In the coming sections, we will discuss work that was done to determine the relationship between magnetic field gradients and our magnetometer response signal, laying the groundwork for determining the magnetometers response to more intricate signals, such as simulated heartbeats.

5.1 Magnetometer Sensitivity Testing

In order to use our setup as an effective magnetometer, we were faced with two major tasks. First, the differential signal produced by the magnetometer is proportional to the magnetic field gradient that we supply, however, we do not know what this constant of proportionality is and thus we must determine it. Secondly, we must find the lowest possible magnetic gradient that we can detect. To address both of these tasks, we generated a magnetic field gradient that had a staircase shape in time, starting with a weak magnetic field gradient and becoming stronger incrementally with each step. By then matching the response curve of the magnetometer to the

gradient field that is applied through linear transformations, we can determine the constant of proportionality that connects our differential signal and the magnetic field gradient.

To match the magnetometers response curve to the generated gradient both a "coarse" and "fine" adjustment method were used. The coarse adjustment utilized linear fitting of average levels of the staircase as displayed in Figure 5.1. The coefficients of this linear fitting were then used to transform the magnetometer response into a "rough" magnetic field gradient. The fine adjustments then consisted of plotting the "rough" gradient alongside the applied field gradient, and modifying parameters to improve the fit by eye and ignore outlier points. Figure 5.2 shows the results of the fitting, and it can be seen that there is good agreement between the applied magnetic field gradients and the magnetic field gradient as detected by the magnetometer. The proportionality factors obtained from each set are listed in 5.1.

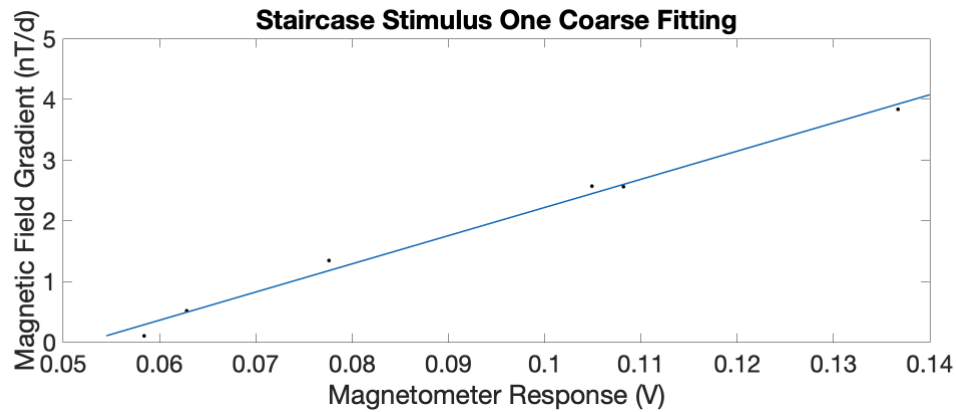Figure 5.1: This graph represents a plot of the averaged levels of the staircase stimulus, versus the averaged level of the magnetometer response over the same time period. A linear fit was then taken, and the result has been displayed in 5.1. This linear fit equation was used alongside others to transform the data in 5.2 from a magnetometer response in arbitrary voltage units, into a magnetic field reading.

Table 5.1: This table contains the fit parameters used for the matching of each magnetometer response in the datasets in 5.2. The linear equation that was used is $B = a \cdot V + c$ where a is the slope, and c is the offset.

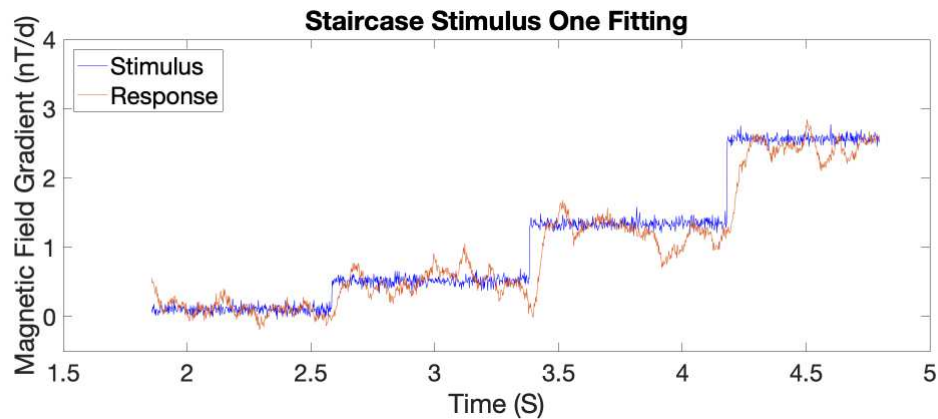| Dataset	Slope (nT/Vd)	Offset (nT/d))
1	44.6	−2.3
2	44	−2.4
3	83.2	−1.99
4	84.3	−2.38

Figure 5.2: This graph displays the results of our linear fitting method, this graph having been fit using the results of Dataset 1. Using the results of this linear fitting, tests can be run using more intricate waveforms, such as heartbeat-like waveforms and tested for their accuracy.

With the magnetometer response now calibrated and translated into a magnetic field gradient, we can determine the minimum detectable magnetic field by finding the general noise level on the signal, as anything lower than this will be washed out in the noise. Based on analysis of each of the steps in the signals, the noise level was determined to be in the range of 100-400pT. Although this puts our magnetometer outside the range of detecting a human heartbeat, it is impressive that our magnetometer was able to detect such weak magnetic fields without the use of averaging or extra filtering.

Chapter 6

Heartbeat-Like Signals

Knowing the resolution limit of our magnetometer, and the conversion factors allows us to now look at heartbeat like signals to test the ability of our magnetometer under more realistic circumstances. To create these signals a custom script in MatLab was created that would create arbitrary waveforms when given an array of points. A second script was then used to create a txt file with the waveform data on it that was sent to our programmable function generator. The response was recorded, and translated using our proportionality factors. Figure 6.1 Shows the results of this conversion when applied to our heartbeat like signals, demonstrating that although there are some promising results here, there is also much work to be done to reduce the noisiness of the signal so that we may detect smaller signals.
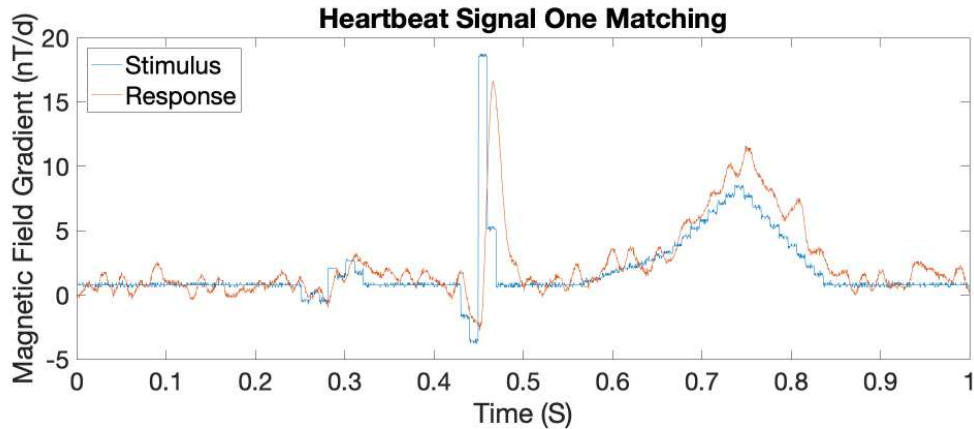
Figure 6.1: The results of converting the heartbeat like signal response from the magnetomter using our conversion factors.The fidelity of the first heartbeat signal test are promising, but the right peak also shows that the slope may be too large. This demonstrates that our calibration of gradient fields does not fully describe all of the factors effecting more complex signals such as simulated heartbeats.

Due to COVID-19 we have been unable to return to the experiment, and the heartbeat signal shown above represents the lowest range of heartbeat-like magnetic field gradients we captured. Based on the work of the previous chapter, our magnetometer should have been able to acquire heartbeat-like magnetic field gradients down to a few hundred pT, close to the level of an actual human heartbeat. Since we are unable to analyze smaller magnetic field gradients, we will consider instead the way in which our magnetometer may be improved to obtain the necessary sensitivity.

6.1 Noise Analysis and Areas of Improvement

Because the sensitivity of our setup is limited by the noise level, de-noising the system is the logical next step for increasing the lowest resolvable signal our magnetometer can acquire. A few areas where noise may be introduced are discussed here. Before we had to leave the experiment, we were experiencing instability with our laser lock, which could be contributing to our system noise. VCSEL lasers themselves

also have a noisy frequency output, which can convert to noise in our magnetometer response. Our tests have been approaching the lower limit of what our current source can output reliably (10mV), thus we may be getting noise from the signal generator. It is also possible that our shielding system is not perfect, or that we are seeing electronic noise contamination of our small signals before they reach the Lock-In amplifier.

Noise introduced by the laser lock instability could certainly be a contributing factor. To get the maximum sensitivity, we try to lock our system at the point on our resonance that has the highest slope, however, this also means that if the system jitters by a small amount, the effect on the system will be proportionally larger than jitter. This kind of interference would likely contribute large spikes in our signal either up or down, and this kind of noise has been seen in our data. Since the VCSEL has frequency noise, this translates to small oscillations around ideal conditions for inducing EIT, which would translate to small changes in our sensitivity response, contributing noise into our system.

Our current source noise may be due to us propagating signals that are on the order of the lowest levels achievable by the generator. Based on examination of the signals we sent in to the magnetometer, this kind of noise has a slightly sporadic nature. When comparing it with the data, the fluctuations in the current source seem to match our noise spectrum in places. At other times it seems that other sources of noise are dominating. However, there is an easy fix to handle noise from our current source that could be improved upon in future work. By introducing a current divider configured such that some percentage of the voltage goes into the magnetometer and the other amount is dumped elsewhere, we could arbitrarily lower the magnitude of signal without having to reach the level of systematic noise from

the function generator.

If our shielding system wasn't perfect it is possible that magnetic fields would begin to interfere from outside. Since our setup is well balanced we should be insensitive to any of these fields that are constant because of our differential detection scheme. However, if any of the interfering magnetic fields had a spatial gradient sufficient to be detected by our magnetometer they would be able to interfere with our detection scheme. Since most ambient magnetic fields come from electrical applications in a laboratory setting, we would expect this noise to have a periodic nature. This kind of noise can be seen within our data, referring back to Figure 6.1, a consistent periodic ripple can be seen in our data, at around 60 Hz frequency, which is a frequency characteristic of noise in any modern laboratory. Noise contamination within cables before they can reach the Lock-In would have a similar nature to the noise that would be introduced by gradients within the magnetic shield, so this is another potential source of that 60 Hz noise. Since we cannot take any physical measures to reduce this noise, we focus on the use of digital filtering methods of noise reduction in post-processing.

6.2   Digital Filtering Methods

Much like electronic filtering methods, digital filtering is a useful method of filtering out noise if you can identify the frequency of the noise's oscillations. We may then be able to improve the performance of our magnetometer by analyzing the frequency spectrum of our signal and removing the noise. Within here, we examine two techniques of digital filtering: brick wall filtering, and RC filtering.
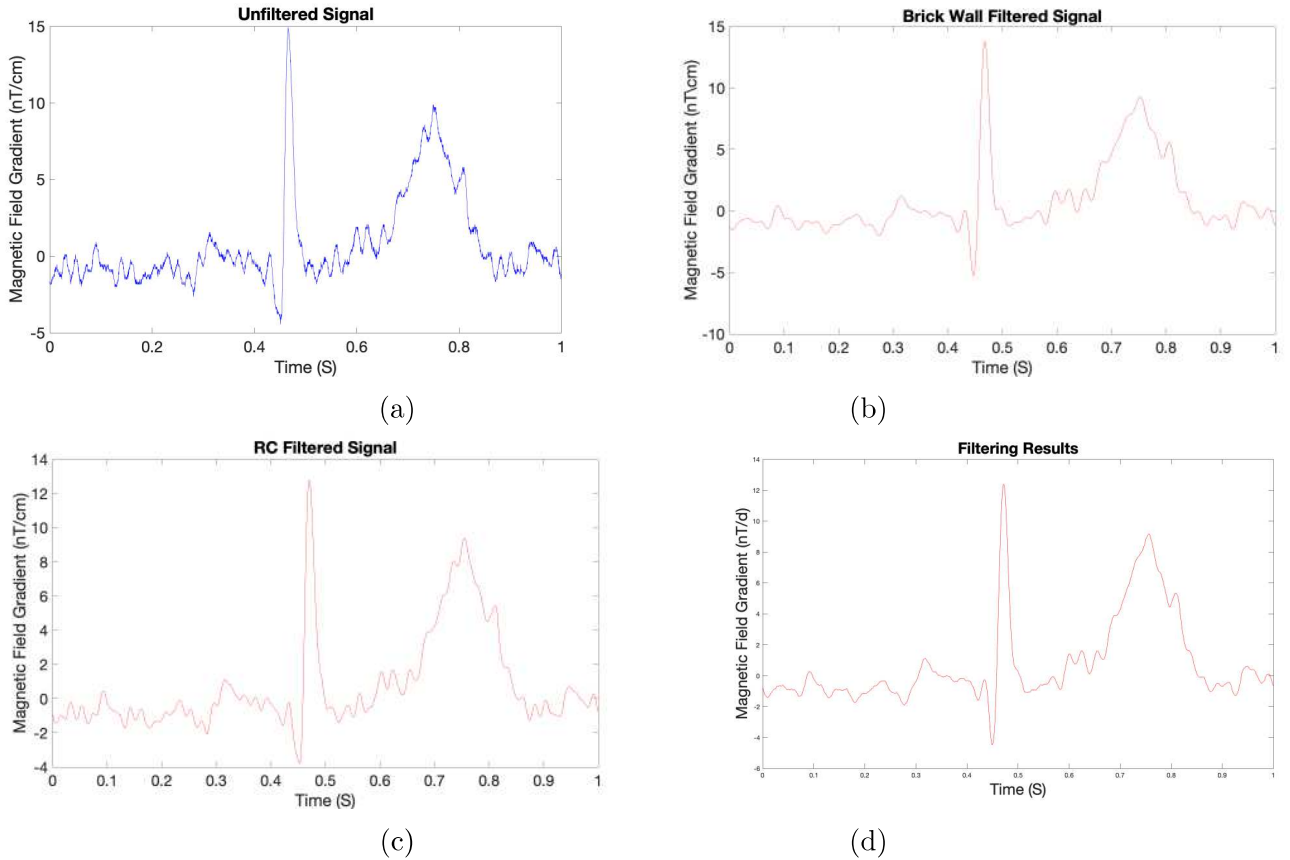
(a)

(b)

(c)

(d)

Figure 6.2: a) An unfiltered trace from one of the heartbeat signals we acquired. b) The same heartbeat trace when filtered using brick wall methods, although noise is reduced, we see the introduction of jagged features. c) Heartbeat trace filtered with an RC filter now, notice that although the signal is now fairly smooth in all locations, the noise has not been reduced as much as in Figure 6.2b. d) The result of our digital filtering on our heartbeat trace, combining both methods of digital filtering. The combination of these methods results in a 25% overall decrease in the noise level

6.2.1 Brick Wall Filtering

Brick Wall Filtering is a technique exclusive to digital filtering, that allows for the decimation of any frequencies that one does not wish to have contributing to the final output. The method by which this is done involves determining the spectrum of fourier frequencies that exist for your signal. Once this is done, we use computational methods to assign a 0 amplitude to any frequencies you do not wish to keep, before inverse fourier transforming the spectrum to recover the filtered signal [18]. An example showing the before and after of a brick wall filtering done on one of our signals is shown in Figure 6.2.
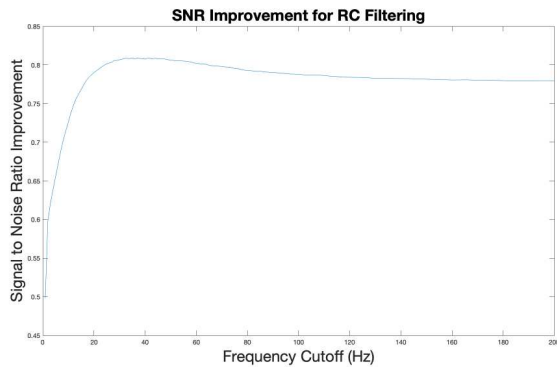
6.2.2 RC Filtering

RC digital filtering, unlike brick wall filtering is analogous to real world RC filtering in the sense that we pick a characteristic frequency at which the amplitude of any frequency we don't want beyond that point will be decreased smoothly by greater than 3db. RC filtering works almost the same way as brick wall filtering, however, instead of assigning zeros on the frequency spectrum, the spectrum is filtered by

$$G = \frac{1}{1 + 1i\frac{f}{f_{3db}}}. \tag{6.1}$$

A before and after example of RC filtering is also shown in Figure 6.2.

6.2.3 Signal to Noise Ratio Analysis

In order to decide on the filtering method, and the cutoff frequencies, we worked to create an optimization algorithm. The method of optimization is fairly simple, the program takes the original signal and computes the signal to noise ration (SNR), then it computes the fourier frequencies. From there the computer iterates through a range of low pass filters, filtering the spectrum at a frequency, inverse transforming
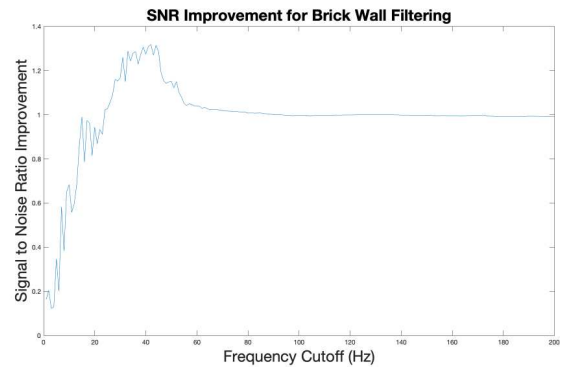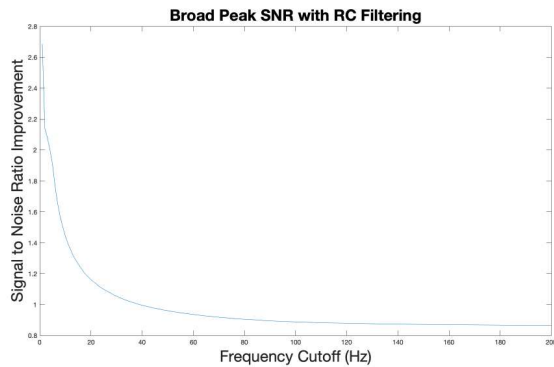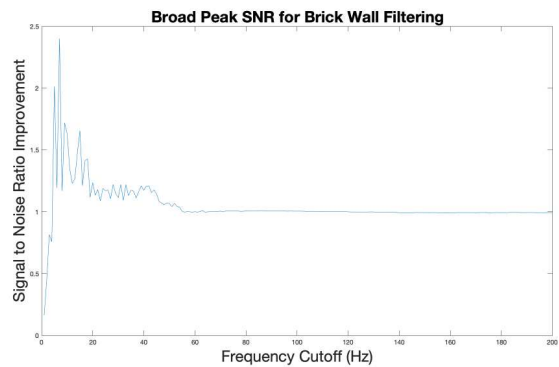
(a)   (b)

Figure 6.3: The optimization results for both digital filtering methods, tested through a range of 1-200Hz. a) shows the results for the RC filter, displaying a smooth curve with a clear maximum SNR in the range of 30-50Hz. b) shows the results for brick wall filtering. A similar curve can be seen here, however, the improvement is greater in magnitude and curve becomes jagged in the range between 0-60Hz. Nonetheless this trace also shows a clear maximum

it, and computing the new SNR. The new SNR is then divided by the original so we have a normalized improvement output. After all this is done, it does the same thing for the next frequency it iterates through until it has covered the full range. This program was used for both brick wall filtering and for RC filtering, and the resulting plots for a range of 1-200Hz cutoff frequencies is shown in Figure 6.3.

An interesting result was also noticed during these SNR trials, which was that the broad peak to the right of the central spike of the heartbeat, as seen in Figure 6.1 also has a spectrum of improvements to its SNR. If the magnetometer were to be used in a diagnostic capacity this may be a useful feature, if the doctor only wished to look at this peak they could filter the data such that the broad peak is prioritized. Using the same program as described above, we examined the SNR improvement over a range of 1-200 Hz cutoff frequencies for low pass brick wall, and RC filters. The SNR improvement at these points is displayed in Figure 6.4.

40

(a)   (b)

Figure 6.4: The optimization results for both digital filtering methods, tested through a range of 1-200Hz. a) shows the results for the RC filter, displaying a smooth curve which tends to increase all the way towards 1 Hz. b) shows the results for brick wall filtering. In this case the SNR improvement seems to be highly variable on the frequency once we evaluate values below 60 Hz, having a maximum value around 5 Hz, and then a rapid drop off that tends towards total loss.

6.2.4   Filtering Results

Considering the example plots, and the SNR analysis, one can see that each method has its own benefits and drawbacks. The brick wall filtering tends to have a better SNR, but examination of the example plots shows that it can introduce new artifacts and oscillation into the signal. The RC filtering produces smoother signals without artifacts, but it tends towards lower SNR values because of the reduction in central peak height it causes. Since there is no clear winner, we decided to use both of them together.

Reconsidering our noise analysis in the previous section, we know that we have some noise in the system that oscillates at ≈ 60 Hz. Since we are sure that this signal has added pesky noise to our system, we set up a band pass brick wall filter to cut this signal out entirely. We then smooth the signal further using the RC filter. The RC filter characteristic frequency was chosen by referencing Figure 6.3a. The result

of these two filters being used together is shown in Figure 6.2d. The combination of these digital filtering methods presents us with a modest 25% decrease in the noise level of the system.

Chapter 7

Conclusions and Next Steps

We have demonstrated a technique with which to measure small magnetic field gradients on top of large magnetic fields. Our technique has the theoretical benefit of not requiring shielding, and does not require cooling, while also being relatively cost-effective. The sensitivity of the magnetometer has been tested, and found to be approximately 400pT, which while not being low enough to detect a hearts magnetic field, would be a reasonable task for whomever will take up the mantle of this project after me. Possible noise sources have also been discussed, and methods of digitally filtering out noise have been shown to have modest success, reducing noise levels by 25%.

Further work on this project is necessary for it to be successful, and my work presents a number of potential areas upon which progress could be built. One of the most practical ways one could potentially increase the sensitivity of this project down to the required level would be by increasing the laser power output. Our VCSEL is notoriously low power, so using a more powerful laser, or applying higher currents would likely result in increases in sensitivity. Additionally, one of the key goals of my work, which unfortunately went unrealized due to COVID-19 was to eventually remove the Rb cell from magnetic shielding and test the abilities of our magnetometer

in a true real world environment.

Bibliography

[1] Andrä Wilfried, Nowak, H. (2007). *Magnetism in Medicine: a handbook.* Weinheim: Wiley-VCH.

[2] Bison, G., Wynands, R., Weis, A. (2003). A Laser-Pumped Magnetometer for the Mapping of Human cardio-magnetic Fields. *Applied Physics B: Lasers and Optics, 76*(3), 325-328. doi: 10.1007/s00340-003-1120-z

[3] K. Cox (2011). Vector Magnetometer Using Rb Vapor. *Undergraduate Honors Theses.* Paper 358.

[4] Bloom, A. L. (1962). Principles of Operation of the Rubidium Vapor Magnetometer. *Applied Optics,1*(1), 61. doi: 10.1364/ao.1.000061

[5] Dupont-Roc, J., Haroche, S., Cohen-Tannoudji, C. (1969). Detection of very weak magnetic fields (10^{-9}gauss) by ^{87}Rb zero-field level crossing resonances. *Physics Letters A, 28*(9), 638-639. doi: 10.1016/0375-9601(69)90480-0

[6] Budker, D., Romalis, M. (2007). Optical Magnetometry. *Nature Physics, 3*(4), 227-234. doi: 10.1038/nphys566

[7] Belfi, J., Bevilacqua, G., Biancalana, V., Cartaleva, S., Dancheva, Y., Moi, L. (2007). Cesium coherent population trapping magnetometer for cardiosignal detection in an unshielded environment. *Journal of the Optical Society of America B, 24*(9), 2357. doi: 10.1364/josab.24.002357

[8] Schwindt, P.D.D, Knappe, S., Shah, V., Hollberg, L., Kitching, J., Liew, L.-A., Moreland, J. (2009). Chip-scale atomic magnetometer. *Applied Physics Letters, 85*, 6409-6411.

[9] Jenkins, Ravn. "Measuring Magnetic Field Gradients using Electromagnetically Induced Transparency in Rb Vapor" (2019). *Undergraduate Honors Theses.* Paper 1370. `https://scholarworks.wm.edu/honorstheses/1370`

[10] Fleischhauer, M., Imamoglu, A., Marangos, J. P. (2005). Electromagnetically Induced Transparency: Optics in Coherent Media. *Reviews of Modern Physics, vol. 77*(2), 633-673. doi:10.1103/revmodphys.77.633.

[11] Griffiths, D. J. (2005), *Introduction to Quantum Mechanics* (2nd ed.). Upper Saddle River, NJ: Pearson Prentice Hall.

[12] Belcher, N., Mikhailov, E.E, Novikova, I. (2009). Atomic clocks and coherent population trapping: Experiments for undergraduate laboratories. *American Journal of Physics, 77*(11), 988-998. doi: 10.1119/1.3120262

[13] Daniel A. Steck, "Rubidium 87 D Line Data,? available online at `http://steck.us/alkalidata` (revision 2.2.1, 21 November 2019).

[14] Sacher Lasertechnik Group: `https://www.sacher-laser.com/applications/overview/absorption_spectroscopy/rubidium_d1.html`

[15] Corwin, K. L., Lu, Z.-T., Hand, C. F., Epstein, R. J., Wieman, C. E. (1998) Frequency-stabilized diode laser with the Zeeman shift in an atomic vapor. *Applied Optics, 37*(15), 3295. doi: 10.1364/ao.37.003295

[16] Yaschuk, V.V., Budker, D., Davis, J. (2000) Laser frequency stabilization using linear magneto-optics. *Review of Scientific Instruments, 71*(2), 341-346. doi: 10.1063/1.1150205

[17] Carlson, J. W. (1988). U.S. Patent No. 4,755,755. Washington, DC: U.S. Patent and Trademark Office.

[18] Mikhailov, E. E. (2018). *Programming with Matlab for Scientists: a Beginners Introduction.* Milton: CRC Press.